SOFT ROBOTS

Robotic surfaces with reversible, spatiotemporal control for shape morphing and object manipulation

Ke Liu[1], Felix Hacker[1,2], Chiara Daraio[1]*

Continuous and controlled shape morphing is essential for soft machines to conform, grasp, and move while interacting safely with their surroundings. Shape morphing can be achieved with two-dimensional (2D) sheets that reconfigure into target 3D geometries, for example, using stimuli-responsive materials. However, most existing solutions lack the ability to reprogram their shape, face limitations on attainable geometries, or have insufficient mechanical stiffness to manipulate objects. Here, we develop a soft, robotic surface that allows for large, reprogrammable, and pliable shape morphing into smooth 3D geometries. The robotic surface consists of a layered design composed of two active networks serving as artificial muscles, one passive network serving as a skeleton, and cover scales serving as an artificial skin. The active network consists of a grid of strips made of heat-responsive liquid crystal elastomers (LCEs) containing stretchable heating coils. The magnitude and speed of contraction of the LCEs can be controlled by varying the input electric currents. The 1D contraction of the LCE strips activates in-plane and out-of-plane deformations; these deformations are both necessary to transform a flat surface into arbitrary 3D geometries. We characterize the fundamental deformation response of the layers and derive a control scheme for actuation. We demonstrate that the robotic surface provides sufficient mechanical stiffness and stability to manipulate other objects. This approach has potential to address the needs of a range of applications beyond shape changes, such as human-robot interactions and reconfigurable electronics.

INTRODUCTION

Biological organisms achieve a remarkable control of shape and functions through a hierarchical architecture of soft tissues (*1*). For example, octopuses use soft tissue to change their shapes for camouflage, locomotion, grasping, and moving objects (*2*); mutable rainfrogs can change skin texture from prickly to smooth when the surrounding environment changes (*3*). Imitating the ability of on-demand shape morphing has been one of the major goals of soft robots, because it is crucial for applications that require motorless and gearless locomotion or interaction with human and other fragile objects (*4*–*8*).

Because the geometry of a three-dimensional (3D) object is effectively defined by its surface, one popular approach to achieve shape morphing is to transform the 3D embedding of a 2D surface, usually starting from a flat one. By prescribing local deformations using active materials (*9*, *10*), it is possible to transform flat sheets into desired curved surfaces, for example, through smooth bending (*11*, *12*) or buckling (*13*–*15*), origami (*16*–*18*) or kirigami (*19*, *20*), and architected materials (*21*–*23*). Shape changes can be actuated by various mechanisms, such as shape memory effect in polymers (*24*, *25*), swelling of hydrogels (*26*–*28*), phase transition of liquid crystal elastomers (LCEs) (*29*–*32*), anisotropy of elastomeric film (*33*), and heterogeneity of layered composite of architected sheets (*34*, *35*). However, for actual applications, several functionalities still need to be demonstrated.

A common limitation of current solutions is their inability to reprogram the target geometry. Ideally, a single surface should be able to transform into different target shapes, at will. To date, much work in the field has focused on sheets preprogrammed with only a single type of 3D shape once manufactured (*11*, *12*, *33*, *34*). A second limitation is that many shape-changing mechanisms can only target a finite set of geometries (*14*, *16*, *20*, *28*). The geometry of a surface must be described by both intrinsic and extrinsic curvatures (i.e., Gaussian and mean curvatures, respectively), resulting from in-plane and out-of-plane deformations (*36*–*38*). For instance, designs with a single active layer can only achieve in-plane deformation. A third limitation is the lack of sufficient mechanical stiffness and stability to perform interactive tasks (*12*, *14*, *21*, *28*). This limitation arises from a difficult trade-off: While the stiffness of a curved surface increases with its thickness (*39*), its shape-morphing capability might be hindered by the increased thickness. Although there are designs that address one or two of these limitations (*26*, *35*, *40*–*44*), soft robots that can simultaneously satisfy all three are rare.

We design a soft robotic surface (*41*, *42*, *45*) that allows for reprogrammable shape morphing into a wide range of smooth 3D geometries, by local control of both intrinsic and extrinsic curvatures. The robotic surface also has sufficient mechanical stiffness and stability to manipulate objects with real-time guidance. The system is assembled as a layered architecture, reminiscent of the musculoskeletal system of some animals (*46*). It consists of two active grids of LCEs supported by a grid of passive ribbons sandwiched between them (Fig. 1, A and B). To actuate shape changes, we use LCEs embedded with stretchable heating coils (Fig. 1C). The actuation of the LCEs is achieved by Joule heating. Each coil is thin and flexible (nichrome wires, 50 μm in diameter), which has minimal effect on the deformation of the robotic surface. Tethering the coils to independent current sources, the network of coils allows for selective and reversible actuation of local deformations. We include two active layers, above and below the passive ribbons, to program both intrinsic and extrinsic curvatures. Synchronized actuation of the two LCE layers leads to in-plane deformations (contractions and expansions) of the surface, whereas differential actuation leads to out-of-plane deformations. Last, we attach cover scales to create a continuous, smooth "skin" surface (Fig. 1B). When not actuated,

[1]Division of Engineering and Applied Science, California Institute of Technology, 1200 E California Blvd, Pasadena, CA 91105, USA. [2]Department of Mechanical and Process Engineering, ETH-Zürich, Rämistrasse 101, 8092 Zürich, Switzerland.
*Corresponding author. Email: daraio@caltech.edu

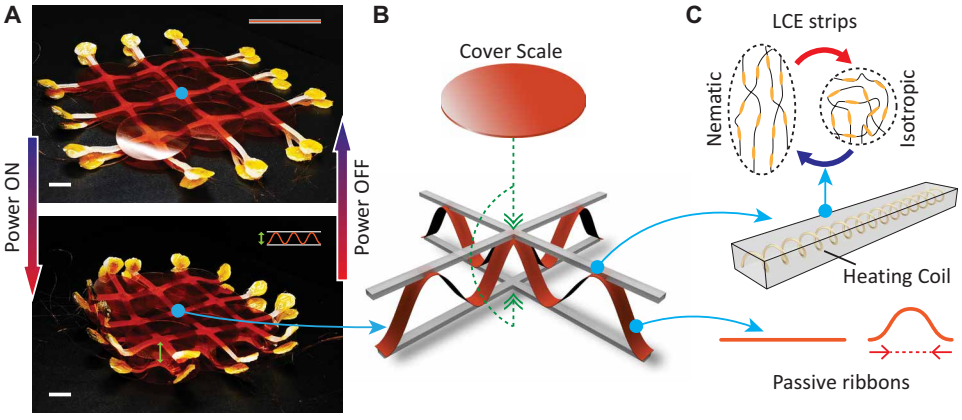

Fig. 1. Design and operation principle of the robotic surface. (**A**) Photographs of the robotic surface. When not actuated, it is a flat, multilayer sheet (top). When current flows through the coils, the robotic surface can be programmed to deform into various 3D shapes (bottom). Scale bars, 10 mm. (**B**) Sketch of the multilayer system including the cover scales (orange), LCE strips (gray), and passive ribbons (red). (**C**) Each actuator is an LCE strip containing a highly stretchable heating coil, connected to a power source. When the LCEs are heated above temperature T_{NI}, the liquid crystal mesogens transition from nematic phase to isotropic phase, driving the LCE strip to contract. The passive ribbons are initially flat and buckle out of plane when the artificial LCE strips contract.

our system is thin and flat, easy to transport and stow. When the LCEs are actuated, the ribbons in the passive layer buckle out of plane (Fig. 1, A and B). In this state, the structure becomes similar to a core sandwich plate, which is known for its high structural efficiency, being lightweight, stiff, and strong (*47*, *48*). The buckled ribbons increase the effective thickness of the robotic surface and keep the structure into a stable, self-stressed state. As the currents are changed through the coils, the LCEs stretch (or contract) and the passive ribbons deform, reaching a new equilibrium state. This new equilibrium state stabilizes the structure in a different geometrical configuration. By harnessing this mechanism, we can continuously transform the shape of the robotic surface and avoid structural instabilities during the shape-morphing process.

Exploiting this on-demand shape morphing, we show the ability of the robotic surface to manipulate objects, such as a ball or passive weights. Despite the fact that the robotic surface only weighs 33 g, it can lift objects that are more than six times its weight without visible distortion or damage.

RESULTS

We demonstrate the robotic surface concept by fabricating a 3 × 3 grid design (Fig. 1A). The active LCE networks (Fig. 1 and fig. S1) are prepared by a two-stage reaction method (*49*). In the first step, the LCE is cured into grid-shaped networks, and the heating coil is integrated inside each LCE strip. In the second step, each strip of the LCE network is stretched to define the nematic length. The grid of passive ribbons is cut from a single Kapton foil using a paper cutter. The two LCE network layers are then glued to the top and bottom of the passive Kapton grid at selected points (Fig. 1B). Last, we attach circular scales over each node of the grid. More details about the fabrication and assembly of our system can be found in Materials and Methods.

Actuation of the LCE strips

We first characterize the actuation response of individual LCE strips, with embedded heating coils (Fig. 2). Each LCE strip has two characteristic lengths, defined by the isotropic and nematic phases of the LCEs. We measured the actuation of an LCE strip by its relative length λ, defined as the ratio of its current length divided by the isotropic length. We denote the relative length in the isotropic phase as λ_I (=1.0) and the relative length in nematic phase as λ_N (>1.0). When a current is applied, the coils heat the LCEs to transition them from the nematic to the isotropic phase, causing a contraction. When the current is shut off, the LCEs cool down and the strips resume their nematic length.

We fabricated nine samples of free-standing LCE strips with embedded coils. All samples have active lengths (fig. S2A) of 80 mm in their isotropic phase and 130.22 ± 8.01 mm (mean ± 1 SD) in nematic phase (Fig. 2B). These dimensions are also preserved in the 3 × 3 grid design for consistency. The amount and speed of the contraction of the LCE strips are a function of the magnitude of input currents. For characterization, we hung individual LCE strips vertically and clamped the lower free ends with paper clips weighing 8.2 g, which apply small tensile forces to prevent curling and twisting during contraction (fig. S2B). In addition, this setup is similar to the working environment of the LCE strips in the robotic surface, because the buckled passive layers also apply tensile forces on the LCE strips in the grid. We applied three different magnitudes of electrical current (0.1, 0.15, and 0.2 A). Considering the resistance of the embedded heating coils, the respective input powers were calculated to be 1.5 ± 0.068, 3.26 ± 0.15, and 5.79 ± 0.27 W. Thermal images (A600 infrared camera, FLIR) were acquired at a rate of 1 Hz to keep track of the instantaneous temperature of the LCE strips during the heating process (Fig. 2A). When the coil is charged by a 0.2-A current, the LCEs reach their isotropic transition temperature T_{NI} (≈70°C) within 10 s, and the strip responds with the fastest contraction, taking about 20 s until full contraction (Fig. 2, A and B). The 0.1-A current requires almost 120 s for full contraction (Fig. 2, A and B). The instantaneous lengths of the LCE strips vary nonlinearly over time, despite a relatively linear increase of temperature, which is explained by the material property of the LCEs (*50*). As the temperature of the LCEs gets close to T_{NI}, the contraction speed of the material gradually slows down. As a result, for actuation of the robotic surface, we chose to operate the system with a 0.2-A current for more rapid contraction and a 0.1-A current for slower contraction. We did not keep a 0.2-A current for more than 30 s to avoid overheating the LCEs.

When the applied currents are above 0.1 A, the LCE strips eventually reach their final isotropic length (i.e., full contraction). To keep each individual strip at a designated length between isotropic and nematic phases, we applied currents with smaller magnitudes, such that the LCEs reached a thermal equilibrium state with temperature always lower than T_{NI}. Figure 2C shows the steady-state lengths of the samples under different input powers, where the samples are tested against six magnitudes of current: 0.09, 0.08, 0.07, 0.06, 0.05, and 0.04 A. Summarizing the experiment, the average

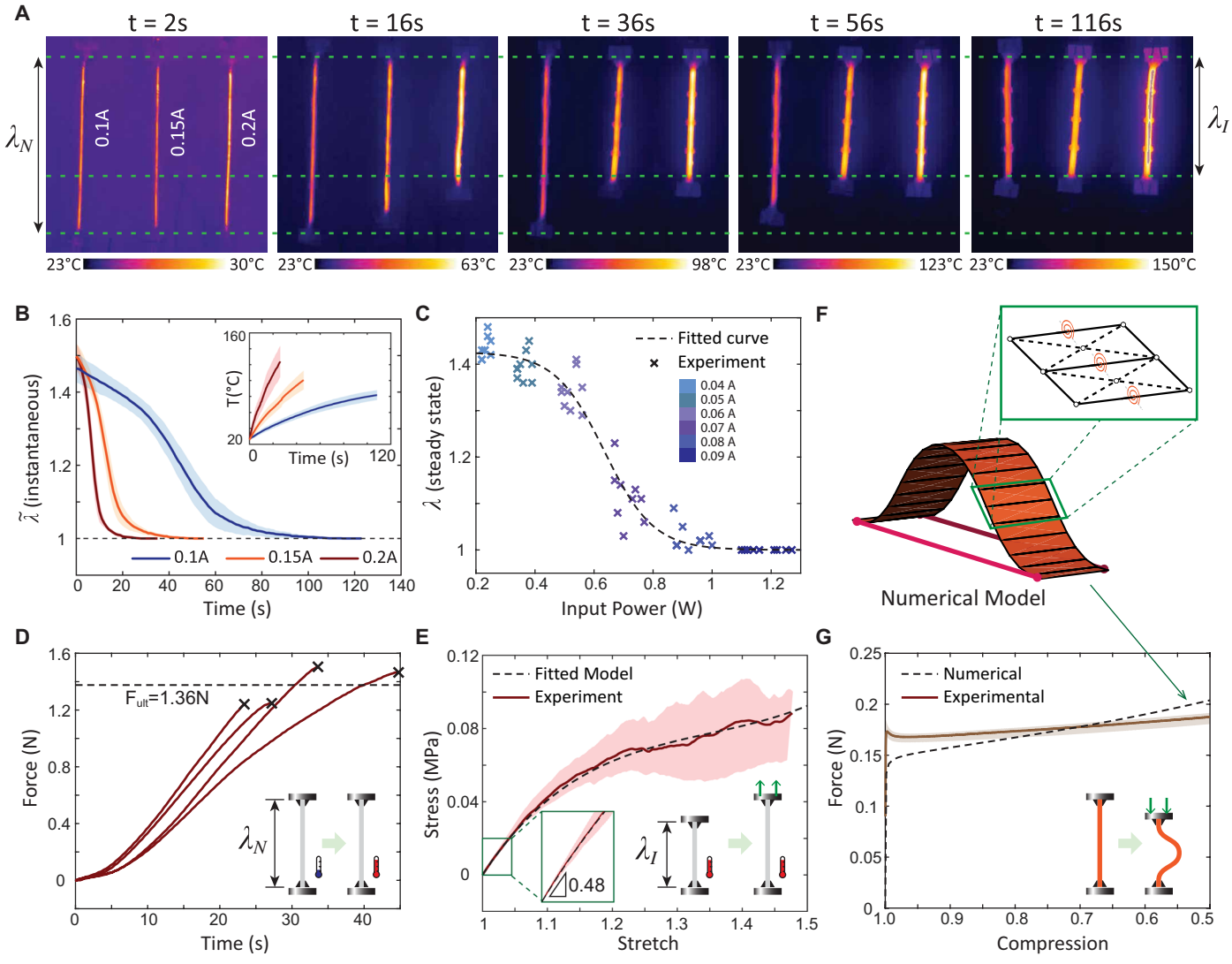

Fig. 2. Characterizations of individual components of the robotic surface. (**A**) Comparison of the actuation behavior of individual LCE strips in response to different applied currents. (**B**) Instantaneous relative lengths ($\tilde{\lambda}$) of the LCE strips under different magnitudes of applied current. The inset shows instantaneous temperature of the LCE strips. The shaded areas extend to 1 SD error. Different colors refer to different applied currents. (**C**) Relative lengths of LCE strips in steady state, charged by different magnitudes of applied currents. The input power is calculated considering the variations in the resistance of the heating coils. (**D**) Actuation force of four LCE strips. This experiment measures the force caused by the actuation of an LCE strip (actuated by a 0.2-A current) with its length fixed at nematic phase (i.e., relative length = λ_N). F_{ult} denotes the average ultimate force before rupture of the LCEs. (**E**) Stress versus stretch (i.e., the ratio of deformed length over initial length) behavior of fully actuated LCE strips (actuated by a 0.2-A current and then kept under a 0.1-A current). The shaded areas extend to extreme values. This experiment measures the force required to stretch an LCE strip in its isotropic phase ($T > T_{NI}$). (**F**) Schematic of the reduced-order model used in numerical simulations. (**G**) Buckling and post-buckling behavior of the passive ribbons, shown by the diagram of force versus compression (i.e., the ratio of deformed length over initial length). The ribbons are subject to fixed-fixed support, as sketched in the inset. The shaded area extends to 1 SD error.

relative length (λ) of an LCE strip in steady state can be empirically calculated by

$$\lambda = \frac{\gamma_1}{1 + e^{\gamma_2(P-\gamma_3)}} + 1 \quad (1)$$

Here, P denotes the input electric power. Performing regression on the experimental data, the parameters γ_1, γ_2, and γ_3 are fitted to be 0.426, 11.97 W^{-1}, and 0.635 W, respectively. Equation 1 is plotted as a dashed line in Fig. 2C. It is noted that the thermal equilibrium temperature of the LCE strips depends on heat dissipation. Different ambient environments would lead to different curves. In this work, the experiments are conducted at room temperature, around 25°C, in air. Maintaining the length of each individual LCE strip is essential for programming the static shape of the robotic surface, because the surface curvature depends on the relative lengths of each strip.

To determine the actuation force of an LCE strip, we held it at its nematic length and applied 0.2-A electrical current until rupture of the LCEs. As shown in Fig. 2D, the actuation force increased from zero to the maximum value in about 30 s for all four samples tested. The ultimate strength of the LCE strip is F_{ult} = 1.36 N on average. In the experiment, when rupture of the LCEs happens, the embedded helical coil is straightened but not broken, as shown in fig. S3 (B and C).

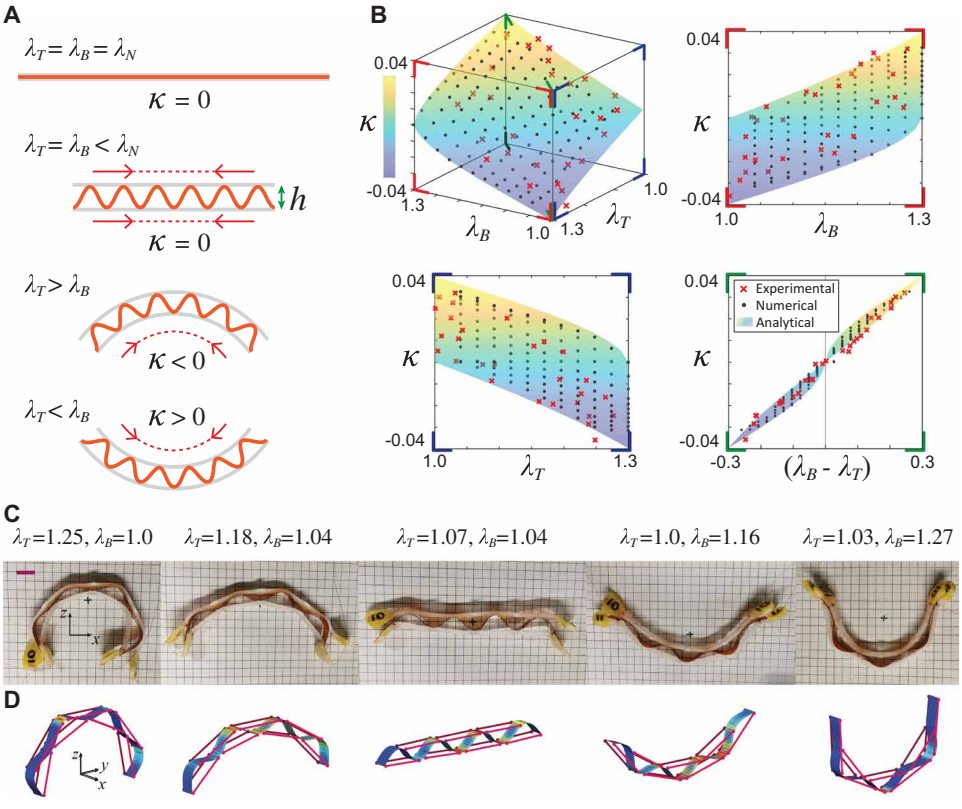

Fig. 3. Curvature of a single composite beam. (**A**) Different lengths of the top and bottom LCE strips lead to different curvatures. (**B**) Curvature (κ) of a single composite beam as a function of lengths of the top (λ_T) and bottom (λ_B) LCE strips. Four different views of the curvature response surface are given. The red crosses are experimental data; the black dots are numerical data; the colored surface is plotted per Eq. 2. (**C**) Photographs of five representative experimental configurations. Scale bar, 10 mm. (**D**) Numerical simulations corresponding to (C).

Such failure scenario is favorable: It keeps the electric circuit unchanged and preserves the integrity of the structure, avoiding cascading failures.

Mechanical properties

We characterize the constitutive behavior of the LCE strips in the isotropic phase ($T > T_{NI}$), which has a linear elastic region at low stretches and a nonlinear softening region at high stretches (Fig. 2E). We note that, even at a relatively large stretch, $\lambda = 1.5$, the LCE strips do not break, because the tensile force is still below F_{ult}, indicating the ability to support large deformations. The stress-extension curve is fitted by an Ogden hyperelastic model (*51*) that is then used in a reduced-order model for fast simulations (Fig. 2F).

We also characterize the mechanical properties of the passive Kapton ribbons (Fig. 2G and fig. S4). The measured average critical buckling load is 0.18 N, and the post-buckling force remains almost constant until 50% compression, which is more than the largest compression ever experienced by the robotic surface under normal working conditions. This implies that a buckled passive ribbon only exerts a small tension (0.18 N) on the actuated LCE strips, which results in at most 5% strain, according to the tensile response of the LCE strips (inset of Fig. 2D). When unloaded, the buckled ribbons return straight again, demonstrating an elastic behavior.

We implement a reduced-order model (Fig. 2F) to perform fast numerical simulations and develop real-time control strategies. In the reduced-order model, the passive ribbons are modeled as a network of springs, including both extensional and torsional springs (i.e., the bar-and-hinge model) (*52*, *53*), in which the extensional springs model the in-plane deformation while the torsional springs model the out-of-plane deformations (see Materials and Methods and note S1 for details). Each LCE strip is modeled as two identical nonlinear extensional springs, to reflect on the finite width of the LCE strips. We fit the constitutive behaviors of the extensional and torsional springs in the reduced-order model using the experimental data. The simulated tensile response of the LCE strips and buckling response of the passive ribbons are shown by the dashed lines in Fig. 2 (E and G, respectively). This ensures that, in the simulations of the entire robotic surface, each individual component behaves just like its physical counterpart. As a result, the reduced-order model allows us to examine how the deformation of an individual LCE segment depends on the deformation of its neighboring segments and to adjust control strategies accordingly.

Curvature of a single composite beam

To control the overall shape of the robotic surface, we need to control the curvature of each element in the grid system (Fig. 3).

The strategy for programming curvature is sketched in Fig. 3A. We denote the length of the top LCE strip as λ_T, the length of the bottom strip as λ_B, and the curvature of the composite beam as κ. Differential contraction of the top and bottom LCE strips leads to different self-stressed states of the structure and thus drives it into different curvatures.

We applied different combinations of electric currents to the top and bottom LCE strips of composite beams. On the basis of the results of our single–LCE strip analysis, by varying the applied current, we can maintain the LCE strip at designated length. The red crosses in Fig. 3B show the experimental results of κ in response to different values of λ_T and λ_B. We observed that the curvature of the composite beams is approximately proportional to the difference of the top and bottom strips' lengths (i.e., $\lambda_T - \lambda_B$). Assuming that the top and bottom LCE strips always lie on a circular arc, the curvature of the beam is derived as a function of λ_T, λ_B, and the beam's thickness h. Because the thickness h depends on the buckling of the passive ribbons under compression, it is mainly a function of λ_T, λ_B, the thickness of the LCE strip t_a, and the straight (pre-buckled) length ℓ_p of the passive ribbon. The curvature can then be estimated by the following formula

$$\kappa = \frac{16\eta(\lambda_T - \lambda_B)}{(\lambda_T + \lambda_B)\left(t_a + \ell_p\sqrt{4 - (\lambda_T + \lambda_B)^2/\lambda_N^2}\right)} \quad (2)$$

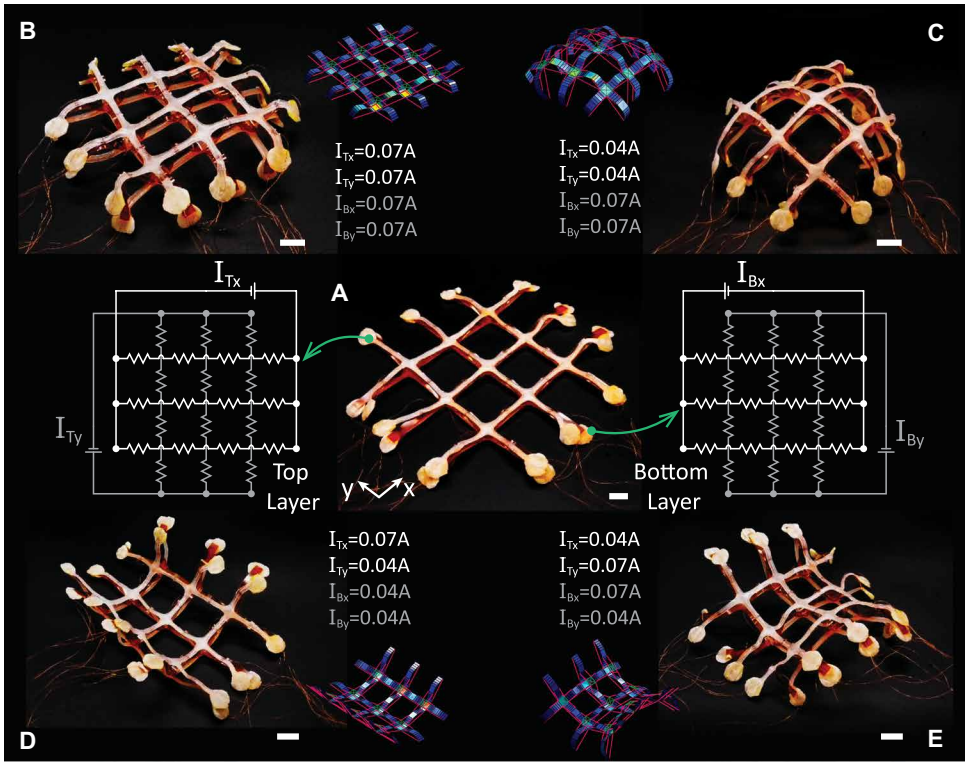

Fig. 4. Different attainable shapes of the robotic surface. (**A**) Initial, flat configuration and schematic of the circuits used to control the LCE strips. (**B**) The actuated table configuration and its required input currents. The inset shows the corresponding configuration from the numerical simulation, obtained by applying $\lambda_{Tx} = \lambda_{Ty} = \lambda_{Bx} = \lambda_{By} = 1.05$. (**C**) The dome shape and its required input currents. The numerically simulated shape was obtained applying $\lambda_{Tx} = \lambda_{Ty} = 1.33$ and $\lambda_{Bx} = \lambda_{By} = 1.05$. (**D**) The dome shape and its required input currents. The numerically simulated shape was obtained applying $\lambda_{Ty} = \lambda_{Bx} = \lambda_{By} = 1.33$ and $\lambda_{Tx} = 1.05$. (**E**) The saddle shape and its required input currents. The numerically simulated shape was obtained applying $\lambda_{Tx} = \lambda_{By} = 1.33$ and $\lambda_{Ty} = \lambda_{Bx} = 1.05$. Scale bars, 10 mm.

where $\eta = 0.57$ is a linear scaling factor fitted by matching experimental data. Detailed derivations are presented in note S2 and fig. S5. Equation 2 and data measured from experiments agree well (Fig. 3B). We experimentally demonstrate the ability of a composite beam to continuously change its curvature on demand, by changing the lengths of the top and bottom LCE strips (Fig. 3C).

To validate the reduced-order model and compare it with experiments (Fig. 3C), we perform quasi-static simulations. We focus on the steady-state configurations, because the shape-morphing process is relatively slow. Quantitative comparisons of the reduced-order model with the experimental data and Eq. 2 are shown in Fig. 3B. Direct comparisons between selected simulated configurations and experimental results are shown in Fig. 3D (cf. Fig. 3C). The numerical simulations agree well with the experiments, capturing the overall curvature as well as the local deformations, validating the accuracy of our reduced-order model. These results serve as a benchmark for establishing control strategies to obtain more complex shapes after combining multiple composite beams.

Programming shape of the robotic surface

In differential geometry, surface curvature is defined by intersecting curves lying on the surface (*36*). This definition is clearly evident in gridshells, for example, which exploit a grid of curved elements to define specific surface curvatures (*54*). Our robotic surface consists of a reconfigurable gridshell, controlled by external currents.

We demonstrate the ability to program different shapes in a 3 × 3 grid design, which has 48 segments of LCE strips that could be controlled individually (24 at the top and 24 at the bottom). For simplicity, we reduce the complexity of the control circuit by connecting the segments in series and parallel, as shown in Fig. 4A. Such an arrangement reduces the independent control variables to four control channels. We denote the average applied current to each LCE strip of the four channels as I_{Tx}, I_{Ty}, I_{Bx}, and I_{By} and the corresponding relative lengths of the LCE strips as λ_{Tx}, λ_{Ty}, λ_{Bx}, and λ_{By}.

Any surface is locally defined by its two principal curvatures and all of their possible combinations, which are dome (+,+), saddle (+,−), cylinder (+/−,0), and flat (0,0) (*36*, *39*). We transform the robotic surface into these four representative shapes (Fig. 4, B to E) to demonstrate its potential to program arbitrary shapes. The symmetric dome shape has a positive Gaussian curvature, and the principal curvatures are both negative with the same magnitude. To obtain a dome shape, all the bottom layer LCE strips need to shrink more than the top strips, such that all the grid lines are programmed with negative curvatures. We perform numerical simulations to estimate the expected shape by defining $\lambda_{Tx} = \lambda_{Ty} = 1.33$ and $\lambda_{Bx} = \lambda_{By} = 1.05$. In the experiment, we first apply 0.1 A to each of the top LCE strips and 0.2 A to the bottom, for initial actuation. After about 20 s, the currents are switched to $I_{Bx} = I_{By} = 0.07$ A and $I_{Tx} = I_{Ty} = 0.04$ A, according to Fig. 2C, to keep the robotic surface at a stable dome shape (Fig. 4C). The principal curvatures at the center joint are $\kappa_x = \kappa_y = -0.017\ \text{mm}^{-1}$

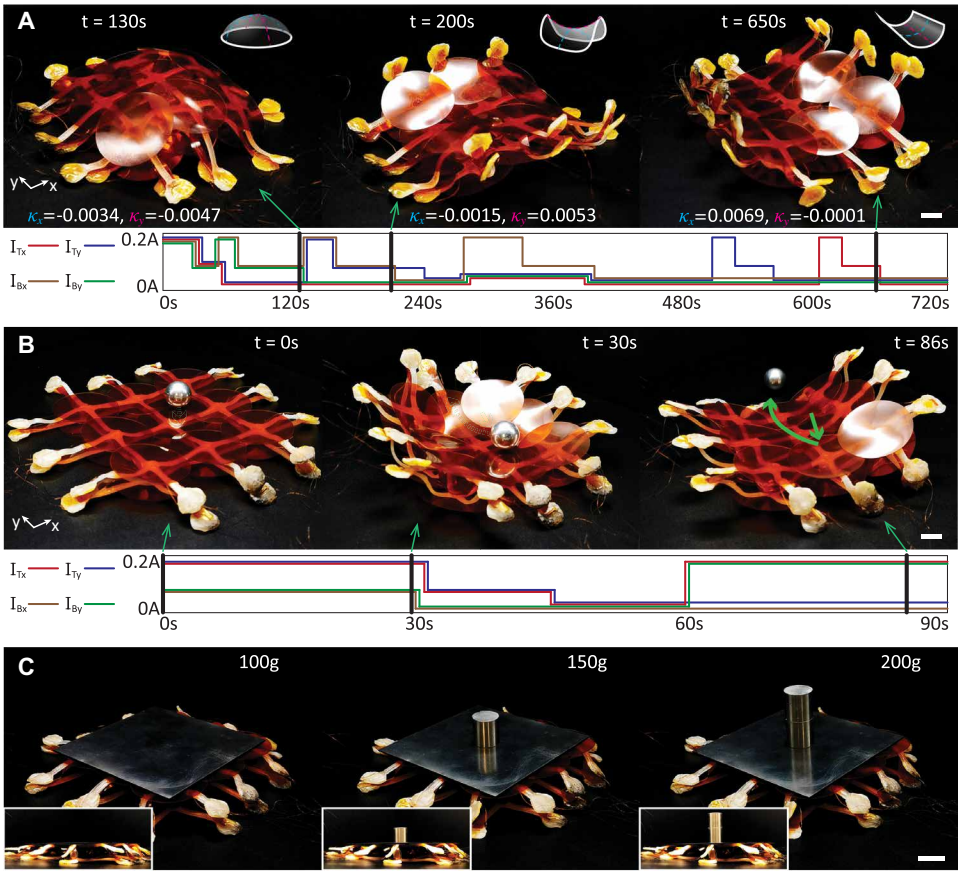

Fig. 5. Robotic surface performing different tasks. (**A**) Sequential shape morphing. The images show selected frames from movie S1. The bottom diagrams show the currents in the four channels used to control the shape evolution. The curvatures are in units of mm $^{-1}$. (**B**) Object manipulation. The images show frames from movie S2, visualizing the motion of an aluminum ball on the surface. The bottom diagrams show the currents in the four channels used to control the shape evolution. (**C**) Weight lifting and holding. The images show frames from movie S3, visualizing the ability to lift and hold different weights (insets show the side view). To control the surface, we applied 0.2 A to all LCE strips. After 25 s, to avoid overheating, currents were reduced to half (0.1 A). Scale bars, 10 mm.

from numerical simulation and $\kappa_x = \kappa_y = -0.016$ mm $^{-1}$ from experiment. The other geometries are programmed similarly, and quantitative comparisons of the resulting curvatures are reported in Materials and Methods. The experimental results agree well with the numerical simulations, despite the differences in boundary conditions and nonidealities in the experiments. For example, the resistances of the embedded heating coils in the LCE strips are not the same, ranging from 126 to 134 ohms, and the magnitude of current flowing through each LCE strip varies around the assigned values. In addition, the LCEs are not perfectly homogeneous among segments of the grid, and thus, Eq. 1 can only provide a rough estimation.

Continuous shape morphing and object manipulation

To transition from a discrete gridshell to a continuous surface, we attach Kapton cover scales to the nodes of the grid. With the scales on, we demonstrated reversible, spatiotemporal control of the surface deformation and show continuous and smooth shape morphing (Fig. 5A and movie S1). We program the current evolution (Fig. 5A, bottom) to allow the surface to evolve from a flat shape to a table, a dome, a saddle, and cylinders. We note that the cover scales, although free to slide relative to one another, increase the overall bending stiffness of the system. This results in ca. 50% smaller achievable principal curvatures, compared with the shapes achievable by the gridshell alone. This effect can be mitigated using thinner cover scales or softer materials.

We also show how the robotic surface can manipulate other objects (Fig. 5B and movie S2). We place an aluminum ball (10 g) on one corner of the surface. To move the ball, we program a bowl shape, so that the ball rolls toward the center of the surface due to gravity. To release the ball from one of the four sides, we program a saddle shape with the downward ramps along the *y* direction. The robotic surface is lightweight (33 g) and not anchored to the table. This makes it difficult to fully control the movement of the ball, because its weight affects the overall posture of the system. We also repeat the same object manipulation with a ping-pong ball and show the ability to release it from another side (movie S2). More precise control of the objects' trajectories and positions could be achieved by controlling the currents in each individual LCE segment, with independent control channels (fig. S6A).

The robotic surface is also able to lift and hold weights. We show this by lifting a 100-g metal pad and then adding two additional 50-g weights (Fig. 5C and movie S3). Even after adding a total weight of 200 g (ca. six times the surface's own weight), no notable deformation was observed. These results suggest that the robotic surface, while being soft and compliant, has sufficient load-bearing ability for object interaction.

DISCUSSION

This paper demonstrates a soft, robotic surface capable of performing continuous and controlled shape morphing. The surface's structure is reminiscent of the skeleton-muscle-skin combination in animals. The proposed shape-morphing mechanism is scale free and could be realized at different dimensions (macro- or microscales). We envision its possible application in haptic technologies, biomedical devices, and/or reconfigurable antennas/lenses (*55*, *56*). It could also enable unconventional technologies such as 3D shape display and remote collaboration, when combined with video screens and other sensory stimuli (*57*). However, the current design leaves room for improvements. For example, to obtain higher shape precision and accuracy, it would be useful to add external sensors that provide feedback for closed-loop control. To achieve higher geometric complexity, it is necessary to add control channels (fig. S6), refine the grid mesh (fig. S7), and explore non-orthogonal meshes. Last, to allow for broader ranges of motion,

untethered actuation would be desirable, e.g., using different LCEs that respond to laser heating, infrared radiation, and/or magnetic fields.

MATERIALS AND METHODS

LCE synthesis

The LCEs were synthesized following a previously reported two-stage thiol-acrylate Michael addition-photopolymerization reaction procedure (*49*). We first dissolved liquid crystal mesogen RM257 [54.6 weight % (wt %), Wilshire Technologies Inc.] and the photo-initiator 2-Hydroxy-4′-(2-hydroxyethoxy)-2-methylpropiophenone (HHMP) (0.35 wt %, Sigma-Aldrich) by toluene (21.8 wt %, Sigma-Aldrich) in a glass vial placed in a hot water bath at 80°C. After the vial was cooled down to room temperature, we added spacer 2,2′-(ethylenedioxy) diethanethiol (EDDET) (12.5 wt %, Sigma-Aldrich), cross-linker PETMP [Pentaerythritol tetrakis (3-mercaptopropionate)] (2.96 wt %, Sigma-Aldrich), and diluted catalyst DPA (7.75 wt %, Sigma-Aldrich) to the vial. Dipropylamine (DPA) was diluted in toluene with a mass ratio of 1:50. The finished solution was then mixed with a vortex mixer for about 20 s. Next, the solution was degassed in a custom-built vacuum chamber for about 45 s at 67.73 kPa until there were no air bubbles. The monomer solution was then injected to a high-density polyethylene mold with grid-shaped channels with heating coils placed inside, as shown in fig. S1A. The cross section of the channel slots is 5 mm wide and 2 mm deep. We then put the mold at room temperature (25°C) for 24 hours. After that, we placed the mold into an 80°C oven with a negative pressure of 69.42 kPa for another 24 hours. The above procedure finished the first stage of polymerization. In the second stage, we stretched the samples to desired lengths to orient the liquid crystal mesogens into a temporary monodomain (fig. S1C). Then, we irradiated the samples by ultraviolet light for 3 min each side to initiate cross-linking between the excess acrylate groups of the LCE network, which stabilizes the alignment of the liquid crystal mesogens.

Fabrication

The grid of passive ribbons, the samples for the buckling test, and the cover scales were cut from 127-μm-thick Kapton films (DuPont de Nemours Inc.) using a Silhouette CAMEO cutter (Silhouette America). The passive ribbons were 7 mm wide, forming a grid-shaped kirigami pattern (Fig. 1B). The nine passive ribbon samples for buckling characterization were 36 mm long and 7 mm wide (fig. S4). The cover scales were circular disks with 50 mm diameter. The heating coil was made of 50-μm-diameter nickel-chrome alloy wires. To fabricate the heating coils, we first tightly wound the nickel-chrome alloy wire (Nichrome 80 wire 44 AWG Gauge, FogsLord) on a 1-mm-diameter steel rod using a drill. Then, the tightly coiled wires were stretched to the designated length. We calculated the length such that the resistance within each segment of the grid is 25 ohms. The coil pitch was determined such that the resistance of the coil is 1.25 ohms/mm on average before stretch. This process is shown in fig. S8. The LCE grids were glued to the grid of passive ribbons using super glue (Krazy Glue).

Thermal and mechanical characterization

As shown in fig. S2, the thermal images were captured by a FLIR A600 infrared camera at 1 Hz for actuation tests. Eventek KPS305D adjustable power supply was used as the power source. The current in each control channel was regulated by a D-Planet LM2596s buck converter. The amount of contraction was read by placing the sample in front of a graph paper and recording the actuation process with a video camera. Stress-strain characteristics were measured using an Instron 5569 universal testing station with a 10-N load cell (fig. S3A).

Geometric characterization

The NextEngine 3D laser scanner (NextEngine Inc.) was used to capture the surface shapes of the complete robotic surface. At the centers of the cover scales, we added reflect tapes to improve tracking of these key points. These nine points were then used to fit a quadratic surface to calculate the principal curvatures in Fig. 5A. Each principal curvature of the grid system (without cover scale) was determined by the radius of the circle passing through the tipping point and two ends of the middle composite beam, for which the coordinates are measured by a ruler. The principal curvatures of the saddle at the center joint were determined as $\kappa_x = -0.010\ \text{mm}^{-1}$ and $\kappa_y = 0.014\ \text{mm}^{-1}$ from numerical simulation and $\kappa_x = -0.012\ \text{mm}^{-1}$ and $\kappa_y = 0.015\ \text{mm}^{-1}$ from experiment. The principal curvatures of the cylinder were $\kappa_x = 0.018\ \text{mm}^{-1}$ and $\kappa_y = 0\ \text{mm}^{-1}$ from numerical simulation and $\kappa_x = 0.017\ \text{mm}^{-1}$ and $\kappa_y = 0\ \text{mm}^{-1}$ from experiment.

Numerical simulation

The numerical simulations were based on a reduced-order model of the robotic surface. The passive ribbons were modeled by the bar-and-hinge model (*52*, *53*). As shown in Fig. 2F and fig. S9, a passive ribbon was discretized to small rectangles, where each of them was modeled as four triangles. The edges of the triangles were considered as bar elements (i.e., extensional springs) to simulate in-plane deformations. The dihedral angles between the triangles were considered as torsional springs to simulate out-of-plane deformations. Each LCE strip was modeled as two identical nonlinear bar elements to reflect on the finite width of the LCE strip. The elastic energy stored in the bars and torsional springs compose the system's energy. To model the contraction of the LCE strips, we gradually reduced the rest lengths, starting from the nematic lengths until reaching the designated relative lengths. We can estimate the required current for each LCE strip by the imposed stretch, using Eq. 1. At each step, after we reduced the rest lengths of the bars, a new equilibrium configuration was found by minimizing the system's energy. Carrying out these steps, we can simulate the shape morphing of the robotic surface. The simulation code was modified from the open source software MERLIN (*52*). Details about the implementation are provided in note S1.

SUPPLEMENTARY MATERIALS

robotics.sciencemag.org/cgi/content/full/6/53/eabf5116/DC1

Note S1. Reduced-order model for numerical simulation.
Note S2. Curvature estimation of a single composite beam.
Fig. S1. Fabrication of the LCE strips.
Fig. S2. Experimental setup for characterization of the actuation behavior of the LCE strips.
Fig. S3. Mechanical testing of the LCE strips.
Fig. S4. Characterization of the buckling and post-buckling behavior of the passive ribbons.
Fig. S5. Derivation of the curvature of the composite beams.
Fig. S6. Numerical demonstration of geometries obtained by controlling each LCE segment independently.
Fig. S7. A robotic surface with denser mesh grid transforms into various shapes.
Fig. S8. Fabrication of the heating coils.
Fig. S9. The reduced-order model for simplified simulation of the robotic surface.
Movie S1. Continuous shape morphing of the robotic surface.

Movie S2. Object manipulation.
Movie S3. Weight lifting.
Movie S4. Numerical simulations using the reduced-order model.
References (*58*–*60*)

REFERENCES AND NOTES

1. K. Oliver, A. Seddon, R. S. Trask, Morphing in nature and beyond: A review of natural and synthetic shape-changing materials and mechanisms. *J. Mater. Sci.* **15**, 10663–10689 (2016).
2. R. T. Hanlon, L.-A. Conroy, J. W. Forsythe, Mimicry and foraging behaviour of two tropical sand-flat octopus species off North Sulawesi, Indonesia. *Biol. J. Linn. Soc.* **93**, 23–38 (2008).
3. J. M. Guayasamin, T. Krynak, K. Krynak, J. Culebras, C. R. Hutter, Phenotypic plasticity raises questions for taxonomically important traits: A remarkable new Andean rainfrog (*Pristimantis*) with the ability to change skin texture. *Zool. J. Linnean Soc.* **173**, 913–928 (2015).
4. M. T. Tolley, R. F. Shepherd, B. Mosadegh, K. C. Galloway, M. Wehner, M. Karpelson, R. J. Wood, G. M. Whitesides, A resilient, untethered soft robot. *Soft Robot.* **1**, 213–223 (2014).
5. M. Wehner, R. L. Truby, D. J. Fitzgerald, B. Mosadegh, G. M. Whitesides, J. A. Lewis, R. J. Wood, An integrated design and fabrication strategy for entirely soft, autonomous robots. *Nature* **536**, 451–455 (2016).
6. G. M. Whitesides, Soft robotics. *Angew. Chem. Int. Ed.* **57**, 4258–4273 (2018).
7. S.-M. Baek, S. Yim, S.-H. Chae, D.-Y. Lee, K.-J. Cho, Ladybird beetle–inspired compliant origami. *Sci. Robot.* **5**, eaaz6262 (2020).
8. B. Mazzolai, C. Laschi, A vision for future bioinspired and biohybrid robots. *Sci. Robot.* **5**, eaba6893 (2020).
9. H. Ko, A. Javey, Smart actuators and adhesives for reconfigurable matter. *Acc. Chem. Res.* **50**, 691–702 (2017).
10. D. Shah, B. Yang, S. Kriegman, M. Levin, J. Bongard, R. Kramer-Bottiglio, Shape changing robots: Bioinspiration, simulation, and physical realization. *Adv. Mater.* , 2002882 (2020).
11. A. A. Bauhofer, S. Krödel, J. Rys, O. R. Bilal, A. Constantinescu, C. Daraio, Harnessing photochemical shrinkage in direct laser writing for shape morphing of polymer sheets. *Adv. Mater.* **29**, 1703024 (2017).
12. S. A. Gladman, E. A. Matsumoto, R. G. Nuzzo, L. Mahadevan, J. A. Lewis, Biomimetic 4D printing. *Nat. Mater.* **15**, 413–418 (2016).
13. Y. Klein, E. Efrati, E. Sharon, Shaping of elastic sheets by prescription of non-Euclidean metrics. *Science* **315**, 1116–1120 (2007).
14. J. Kim, J. A. Hanna, M. Byun, C. D. Santangelo, R. C. Hayward, Designing responsive buckled surfaces by halftone gel lithography. *Science* **335**, 1201–1205 (2012).
15. H. Aharoni, Y. Xia, X. Zhang, R. D. Kamien, S. Yang, Universal inverse design of surfaces with thin nematic elastomer sheets. *Proc. Natl. Acad. Sci.* **115**, 7206–7211 (2018).
16. E. Hawkes, B. An, N. M. Benbernou, H. Tanaka, S. Kim, E. D. Demaine, D. Rus, R. J. Wood, Programmable matter by folding. *Proc. Natl. Acad. Sci.* **107**, 12441–12445 (2010).
17. K. Liu, T. Tachi, G. H. Paulino, Invariant and smooth limit of discrete geometry folded from bistable origami leading to multistable metasurfaces. *Nat. Commun.* **10**, 4238 (2019).
18. J. Cui, T.-Y. Huang, Z. Luo, P. Testa, H. Gu, X.-Z. Chen, B. J. Nelson, L. J. Heyderman, Nanomagnetic encoding of shape-morphing micromachines. *Nature* **575**, 164–168 (2019).
19. F. Wang, X. Guo, J. Xu, Y. Zhang, C. Q. Chen, Patterning curved three-dimensional structures with programmable kirigami designs. *J. Appl. Mech.* **84**, 061007 (2017).
20. P. Celli, C. McMahan, B. Ramirez, A. Bauhofer, C. Naify, D. Hofmann, B. Audoly, C. Daraio, Shape-morphing architected sheets with non-periodic cut patterns. *Soft Matter* **14**, 9744–9749 (2018).
21. W. J. Boley, W. M. van Rees, C. Lissandrello, M. N. Horenstein, R. L. Truby, A. Kotikian, J. A. Lewis, L. Mahadevan, Shape-shifting structured lattices via multimaterial 4d printing. *Proc. Natl. Acad. Sci. U.S.A.* **116**, 20856–20862 (2019).
22. L. Jin, A. E. Forte, B. Deng, A. Rafsanjani, K. Bertoldi, Kirigami-inspired inflatables with programmable shapes. *Adv. Mater.* **32**, 2001863 (2020).
23. P. Dieleman, N. Vasmel, S. Waitukaitis, M. van Hecke, Jigsaw puzzle design of pluripotent origami. *Nat. Phys.* **16**, 63–68 (2020).
24. Y. Mao, Z. Ding, C. Yuan, S. Ai, M. Isakov, J. Wu, T. Wang, M. L. Dunn, H. J. Qi, 3D printed reversible shape changing components with stimuli responsive materials. *Sci. Rep.* **6**, 24761 (2016).
25. J. Wu, C. Yuan, Z. Ding, M. Isakov, Y. Mao, T. Wang, M. L. Dunn, H. J. Qi, Multi-shape active composites by 3D printing of digital shape memory polymers. *Sci. Rep.* **6**, 24224 (2016).
26. C. Yu, Z. Duan, P. Yuan, Y. Li, Y. Su, X. Zhang, Y. Pan, L. L. Dai, R. G. Nuzzo, Y. Huang, H. Jiang, J. A. Rogers, Electronically programmable, reversible shape change in two- and three-dimensional hydrogel structures. *Adv. Mater.* **25**, 1541–1546 (2013).
27. S.-J. Jeon, A. W. Hauser, R. C. Hayward, Shape-morphing materials from stimuli-responsive hydrogel hybrids. *Acc. Chem. Res.* **50**, 161–169 (2017).
28. A. Nojoomi, H. Arslan, K. Lee, K. Yum, Bioinspired 3D structures with programmable morphologies and motions. *Nat. Commun.* **9**, 3705 (2018).
29. A. Kotikian, R. L. Truby, J. W. Boley, T. J. White, J. A. Lewis, 3D printing of liquid crystal elastomeric actuators with spatially programed nematic order. *Adv. Mater.* **30**, 1706164 (2018).
30. M. J. Ford, C. P. Ambulo, T. A. Kent, E. J. Markvicka, C. Pan, J. Malen, T. H. Ware, C. Majidi, A multifunctional shape-morphing elastomer with liquid metal inclusions. *Proc. Natl. Acad. Sci. U.S.A.* **116**, 21438–21444 (2019).
31. Y.-Y. Xiao, Z.-C. Jiang, X. Tong, Y. Zhao, Biomimetic locomotion of electrically powered "Janus" soft robots using a liquid crystal polymer. *Adv. Mater.* **31**, 1903452 (2019).
32. A. Kotikian, C. McMahan, E. C. Davidson, J. M. Muhammad, R. D. Weeks, C. Daraio, J. A. Lewis, Untethered soft robotic matter with passive control of shape morphing and propulsion. *Sci. Robot.* **4**, eaax7044 (2019).
33. J. H. Pikul, S. Li, H. Bai, R. T. Hanlon, I. Cohen, R. F. Shepherd, Stretchable surfaces with programmable 3d texture morphing for synthetic camouflaging skins. *Science* **358**, 210–214 (2017).
34. R. Guseinov, C. McMahan, J. Pérez, C. Daraio, B. Bickel, Programming temporal morphing of self-actuated shells. *Nat. Commun.* **11**, 237 (2020).
35. T. L. Buckner, R. A. Bilodeau, S. Y. Kim, R. Kramer-Bottiglio, Roboticizing fabric by integrating functional fibers. *Proc. Natl. Acad. Sci.* **117**, 25360–25369 (2020).
36. M. P. Do Carmo, *Differential Geometry of Curves and Surfaces* (Prentice-Hall, 1976).
37. G. W. Jones, L. Mahadevan, Optimal control of plates using incompatible strains. *Nonlinearity* **28**, 3153–3174 (2015).
38. W. M. van Rees, E. Vouga, L. Mahadevan, Growth patterns for shape-shifting elastic bilayers. *Proc. Natl. Acad. Sci.* **114**, 11597–11602 (2017).
39. C. R. Calladine, *Theory of Shell Structures* (Cambridge Univ. Press, 2010).
40. T. H. Ware, M. E. McConney, J. J. Wie, V. P. Tondiglia, T. J. White, Voxelated liquid crystal elastomers. *Science* **347**, 982–984 (2015).
41. A. A. Stanley, A. M. Okamura, Controllable surface haptics via particle jamming and pneumatics. *IEEE Trans. Haptics* **8**, 20–30 (2015).
42. L. Chen, C. Yang, H. Wang, D. T. Branson, J. S. Dai, R. Kang, Design and modeling of a soft robotic surface with hyperelastic material. *Mech. Mach. Theory* **130**, 109–122 (2018).
43. A. S. Kuenstler, M. Lahikainen, H. Zhou, W. Xu, A. Priimagi, R. C. Hayward, Reconfiguring gaussian curvature of hydrogel sheets with photoswitchable host-guest interactions. *ACS Macro Lett.* **9**, 1172–1177 (2020).
44. J. Chen, J. Huang, H. Zhang, Y. Hu, A photoresponsive hydrogel with enhanced photoefficiency and the decoupled process of light activation and shape changing for precise geometric control. *ACS Appl. Mater. Interfaces* **12**, 38647–38654 (2020).
45. Y. Wang, C. Frazelle, R. Sirohi, L. Li, I. D. Walker, K. E. Green, Design and characterization of a novel robotic surface for application to compressed physical environments, in *2019 International Conference on Robotics and Automation (ICRA)* (IEEE, 2019), pp. 102–108.
46. D. E. Ingber, V. C. Mow, D. Butler, L. Niklason, J. Huard, J. Mao, I. Yannas, D. Kaplan, G. Vunjak-Novakovic, Tissue engineering and developmental biology: Going biomimetic. *Tissue Eng.* **12**, 3265–3283 (2006).
47. N. Wicks, J. W. Hutchinson, Optimal truss plates. *Int. J. Solids Struct.* **38**, 5165–5183 (2001).
48. K. P. Dharmasena, H. N. G. Wadley, K. Williams, Z. Xue, J. W. Hutchinson, Response of metallic pyramidal lattice core sandwich panels to high intensity impulsive loading in air. *Int. J. Impact Eng.* **38**, 275–289 (2011).
49. M. O. Saed, A. H. Torbati, D. P. Nair, C. M. Yakacki, Synthesis of programmable main-chain liquid-crystalline elastomers using a two-stage thiol-acrylate reaction. *J. Vis. Exp.* **107**, e53546 (2016).
50. M. Warner, E. M. Terentjev, *Liquid Crystal Elastomers* (Oxford Univ. Press, 2007).
51. R. W. Ogden, *Non-Linear Elastic Deformations* (Dover Publications, 1997).
52. K. Liu, G. H. Paulino, Nonlinear mechanics of non-rigid origami: An efficient computational approach. *Proc. R. Soc. A* **473**, 20170348 (2017).
53. E. T. Filipov, K. Liu, T. Tachi, M. Schenk, G. H. Paulino, Bar and hinge models for scalable analysis of origami. *Int. J. Solids Struct.* **124**, 26–45 (2017).
54. C. Baek, A. O. Sageman-Furnas, M. K. Jawed, P. M. Reis, Form finding in elastic gridshells. *Proc. Natl. Acad. Sci.* **115**, 75–80 (2018).
55. M. Rashed Khan, G. J. Hayes, J.-H. So, G. Lazzi, M. D. Dickey, A frequency shifting liquid metal antenna with pressure responsiveness. *Appl. Phys. Lett.* **99**, 013501 (2011).
56. S. A. Nauroze, L. S. Novelino, M. M. Tentzeris, G. H. Paulino, Continuous-range tunable multilayer frequency-selective surfaces using origami and inkjet printing. *Proc. Natl. Acad. Sci. U.S.A.* **115**, 13210–13215 (2018).
57. D. Leithinger, S. Follmer, A. Olwal, H. Ishii, Physical telepresence: Shape capture and display for embodied, computer-mediated remote collaboration, in *Proceedings of the 27th Annual ACM Symposium on User Interface Software and Technology*, UIST '14 (Association for Computing Machinery, 2014), pp. 461–470.
58. B. Audoly, Y. Pomeau, *Elasticity and Geometry: From Hair Curls to the Non-Linear Response of Shells* (Oxford Univ. Press, 2010).
59. S. Matsutani, Euler's elastica and beyond. *J. Geom. Symmetry Phys.* **17**, 45–86 (2010).

60. A. Liakou, E. Detournay, Constrained buckling of variable length elastica: Solution by geometrical segmentation. *Int. J. Non Linear Mech.* **99**, 204–217 (2017).

Acknowledgments: We extend our appreciation to V. Lee for helping with the synthesis of LCEs and to R. Bai and P. Ermanni for helpful discussions. **Funding:** We acknowledge financial support from the U.S. NSF CSSI grant number 1835735 and from the Army Research Office (ARO) grant W911NF-17-1-0147. Travel funds to F.H. were provided by the financial aid office of ETH-Zürich. **Author contributions:** K.L. and C.D. designed the research. F.H. and K.L. performed all experiments and data postprocessing. K.L. conducted theoretical derivations and numerical simulations. C.D. supervised the project. All the authors participated in the analysis of the results and in the writing of the paper. **Competing interests:** The authors declare that they have no competing interests. **Data and materials availability:** All data needed to evaluate the conclusions in the paper are present in the paper or the Supplementary Materials. The code for numerical simulations has been deposited in the GitHub repository: https://github.com/Daraio-lab/RoboticSurface_SciRob_LiuK.

Submitted 31 October 2020
Accepted 16 March 2021
Published 7 April 2021
10.1126/scirobotics.abf5116

Citation: K. Liu, F. Hacker, C. Daraio, Robotic surfaces with reversible, spatiotemporal control for shape morphing and object manipulation. *Sci. Robot.* **6**, eabf5116 (2021).

Robotic surfaces with reversible, spatiotemporal control for shape morphing and object manipulation

Ke Liu, Felix Hacker and Chiara Daraio

Sci. Robotics **6**, eabf5116.
DOI: 10.1126/scirobotics.abf5116